Gu, H., Li, S., Pavier, M., Attallah, M. M., Paraskevoulakos, C., & Shterenlikht, A. (2019). Fracture of three-dimensional lattices manufactured by selective laser melting. *International Journal of Solids and Structures*, *180-181*, 147-159. https://doi.org/10.1016/j.ijsolstr.2019.07.020

Fracture of three-dimensional lattices manufactured by selective laser melting

Huaiyuan Gu[a,*], Sheng Li[b], Martyn Pavier[a], Moataz M. Attallah[b], Charilaos Paraskevoulakos[c], Anton Shterenlikht[a]

[a] *Department of Mechanical Engineering, University of Bristol, Queen's Building, University Walk, Bristol BS8 1TR, UK*
[b] *School of Metallurgy and materials, The University of Birmingham, Birmingham B15 2TT, UK*
[c] *Interface Analysis Centre,School of Physics,University of Bristol, HH Wills Laboratory,Bristol,BS8 1TL*

Abstract

Experimentation has been performed to measure the fracture behaviour of three-dimensional lattices manufactured using a Selective Laser Melting (SLM) technique. Specimens have been designed using a compact tension (CT) geometry with different lattice orientations and fabricated from a relatively brittle Aluminum alloy. The toughness has been measured and an increase in fracture resistance has been observed during crack extension. The influence of lattice orientation has been demonstrated, which shows that a change in orientation will result in a different crack path, but the effect on toughness is small. Finally, the significance of specimen size on toughness measurement has been investigated using finite element (FE) analysis. The results show that the experimentally measured result have overestimated the fracture toughness of the lattice specimens by approximately 10% due to the insufficiently large specimen size.

Keywords: Lattices, lattice orientation, fracture toughness, fracture test, FE analysis

*Corresponding author
Email address: hg1740@bristol.ac.uk (Huaiyuan Gu)

1. Introduction

The periodic lattice structures are used in a rang of engineering and medical applications[1, 2, 3, 4]. Unique mechanical properties can be achieved with very low density by manipulating topology and size of unit cell[5, 6, 7]. With advanced additive manufacturing(AM) technique, complex lattice structures can be directly manufactured from computer designed models.

Generally lattices with high nodal connectivity such as two-dimensional triangular lattices and octet-truss lattices[8] exhibit high strength to density ratio and are more suitable for structural elements. Theoretical work has been carried out to allow the prediction of macroscopic mechanical properties including stiffness, strength and toughness from structural properties such as nodal connectivity, cell size,l, and relative density,$\overline{\rho}$. For example fracture toughness of lattices can be expressed as:

$$K_{IC} = D\overline{\rho}^{d}\sigma_f\sqrt{l} \tag{1}$$

where D and d are constants dependent on lattice topology[9, 10, 11, 12].

A lattice orientation effect has also been demonstrated. It was found that strength and fracture toughness of two-dimensional triangular lattices vary remarkably with orientation, although the modulus was almost isotropic[13]. The validity of using linear elastic fracture mechanics(LEFM)technique on lattices has been assessed for two-dimensional topologies, where a reasonable results were achieved for lattices with sufficiently large numbers of cells and a large crack size [12, 13, 14].

Three-dimensional lattices are used as the core of sandwich panels due to their superior compressive performance and energy absorbing characteristic [15, 16, 17]. Recent studies have explored mechanical properties of octet-truss lattices [18].

Additive manufacturing technique is one of the most popular way for fabrication of three-dimensional lattice structures. Laser-based Powder Bed Fusion (L-PBF) for example, also known as Selective Laser Melting (SLM), has drawn

a lot of interests due to its unique ability of manufacturing three-dimensional complex lattices with improved efficiency compared to other methods. Qiu et al. [19] investigated processing conditions such as laser powder and laser scanning speed on lattice qualities including dimensional accuracy and porosity. Wauthle et al.[20] investigated factors in the manufacturing process including build orientation and heat treatment which have a significant effect on mechanical properties.

In previous work, mechanical testing has been conducted on lattices produced using AM technique. The compressive behaviour and failure modes of several periodic lattices have been measured[21, 22]. The influence of heat treatment on lattice crushing behaviour and energy absorbing has been examined by Maskery et al.[23]. Burton.et al.[24] investigated compressive and fatigue performances of lattices designed for medical implants. The failure mechanism of gyroid lattice under uniaxial tension and three point bending load was experimentally characterised by Alsalla et al.[25].

In work described in this paper, the fracture behaviour of octet-truss lattice have been explored at different orientations, where the lattice is obtained by stacking up tetrahedral truss structures with interconnecting triangular lattice in each layer. The structure configuration is shown in Fig. 1. Based on the unit cell geometry, the relative density,$\overline{\rho}$, of the lattice can be related to strut dimensions as:

$$\overline{\rho} = 6\sqrt{2}\pi(\frac{r}{l})^2 \tag{2}$$

Where r and l are radius and length of strut. Specimens have been designed using compact tension geometry and manufactured by SLM technique. X-ray computed tomography(XCT) has been conducted to assess specimen qualities including strut dimensions and porosity. Fracture properties such as toughness, crack path and load-displacement curves have been measured. Finally, FE analysis has been performed to demonstrate the effect of specimen size and assess the validity of the results measured from experiment.

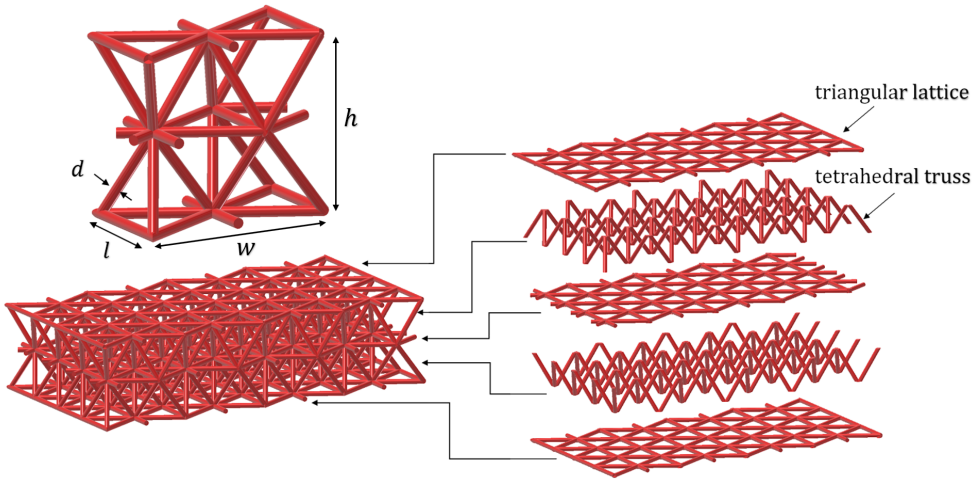

Figure 1: Structure configuration of octet-truss lattice

2. Experiment

2.1. Specimen design

Compact tension (CT) fracture specimens have been manufactured with two different lattice orientations. These two orientations are referred to as orientation-y and orientation-z and are shown in Fig.2. The CT specimen geometry was based on the ASTM-E399 standard [26].

In Fig.2, the X, Y, Z axes represent the global coordinates of the specimen geometry, while the x, y, z axes represent the local coordinates of the lattice unit cell. Each local coordinate is specified with a Miller indices, which is given based on the coordinate system illustrated from the previous work [27]. For orientation-y specimens, the y-axis in the local coordinate system is parallel to the loading direction, which is along the Y-axis of the global coordinate system. For orientation-z specimens, the cell orientation was rotated 90° about the x-axis so that the z-axis in the local coordinate system is parallel to the loading direction.

The nominal strut length,l, and diameter,d, were equal to 5 mm, and 0.5 mm. The specimen sizes shown in Fig.3 were chosen to achieve a high enough

ratio of W to l to allow analysis using the techniques of fracture mechanics [13]. Two solid rings were built around the pin holes to strengthen the local structure. Two thin plates with knife edges were bonded to each specimen to allow measurement of crack mouth opening displacement(CMOD).

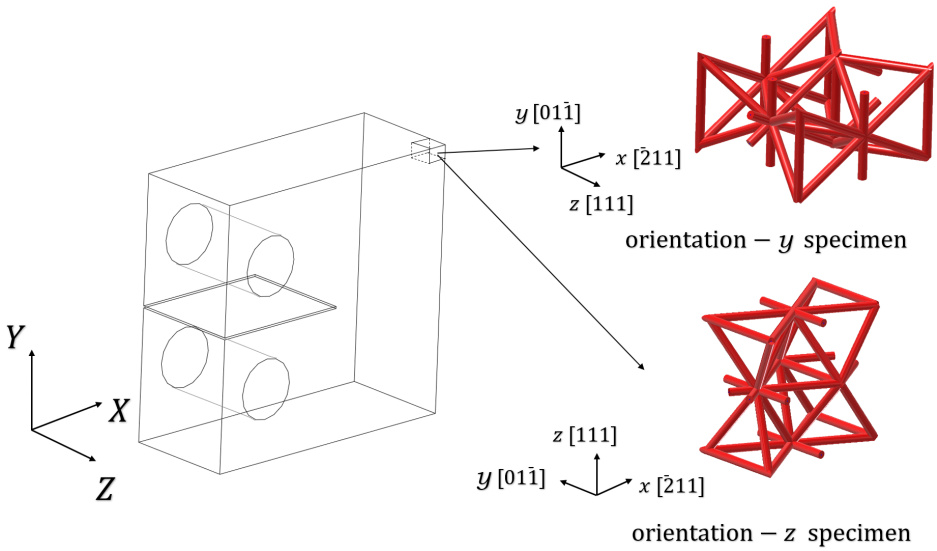

Figure 2: Definition of specimen orientations

2.2. Specimen manufacturing

Fig.4 shows the specimens which are manufactured using a SLM solution Gmbh SLM500HL L-PBF machine equipped with 2 sets of 1000W laser, 2 sets of 400W laser and 2 sets of scanning lens systems. The 400W laser was chosen for the lattice manufacturing to ensure a better geometry accuracy due to its small spot size of about $90\mu m$ in diameter. A205 aluminium alloy metal powder was used for specimen production[28]. The metal powder was produced by EIGA (Electrode induction melting gas atomiser) by the TLS Company with particle sizes ranging from $15\mu m$ to $53\mu m$.

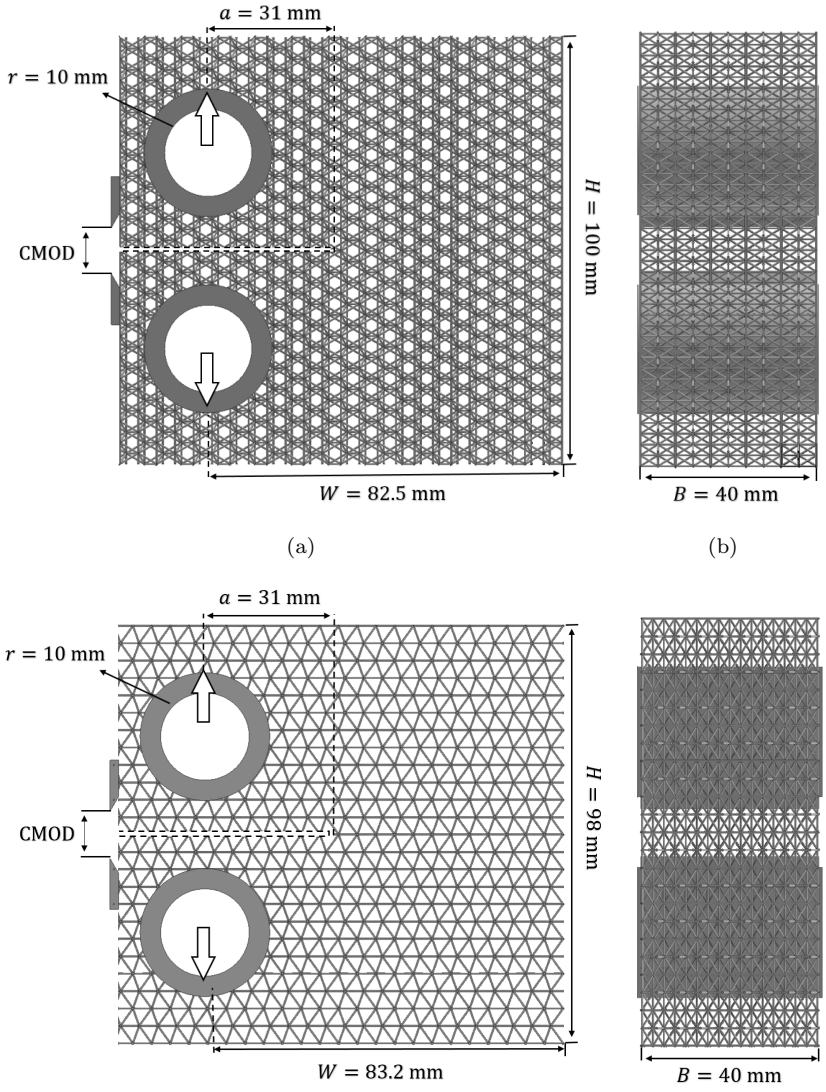

Figure 3: Designed specimens geometry with $\frac{a}{W} = 0.38$: (a)(b) are side and front view of orientation-y specimen;(c)(d) are that for orientation-z specimen

Specimens were produced at a constant laser scanning speed of 1650mm/s with laser power of 350W. 150°C preheating was used to reduce residual stress during manufacturing and achieve good density[29]. The substrate and build chamber were preheated to 150°C for 3 hours and maintained at the same temperature during the building process to reduce residual stress developed in the specimens. The oxygen level was controlled up to lower than 0.17% by flooding Argon into the chamber so as to avoid formation of oxides.

After manufacturing, specimens were removed from the substrate and subjected to heat treatment. Specimens were solution treated at 521°C for 17 hours followed by water quenching which aimed to homogenise the micro-structure and chemical composition, especially for copper and magnesium elements. Aging treatment was then conducted for 22 hours at 170°C to allow precipitation of Ω and θ strengthening phases [30]. Finally, a pre-crack was introduced into each specimen using wire Electrical Discharge Machining (EDM). The EDM technique was found to be able to produce a smooth and clean cut into the specimens without damage or deformation of struts in the vicinity of the cutting path. A wire of a diameter of 0.1mm was chosen to enable accurate crack location.

2.3. X-ray computed tomography

X-ray computed tomography has been conducted to measure the strut dimensions. The size of the specimen was found to be too large to allow images to be constructed of with a reasonable resolution. Therefore, a scan was performed on a small lattice cube with edge length 26.5mm, shown in Fig.5(a), designed with identical strut dimensions and manufactured in the same chamber as the CT specimens.

X-ray computed tomography was performed using a Zeiss X-Radia 520 Versa scanner. Both low and high magnification scans were performed to measure the strut length,l, and diameter,d, shown in Fig.5 and evaluate the porosity shown in Fig. 6 respectively. The resolution of the low magnification scan was 25.22 μm/pixel, while the corresponding one for the high magnification scan was 3.57

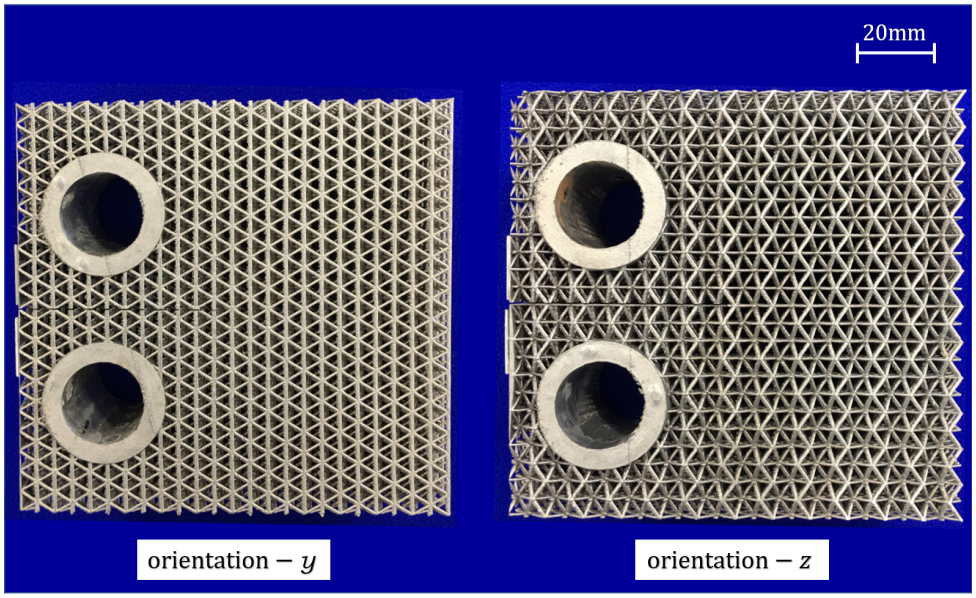

Figure 4: Specimen manufactured by SLM technique

μm/pixel.

The strut dimensions were selectively measured on a proportion of the 2D images (Orthoslices) used to stack the 3D volume of the probed material (the low magnification scan). Image processing software Avizo[31] was used for processing. A significant surface roughness was noticed on the upper surface of the strut, as shown in Fig.6, caused by the non-melted particles loosely attached to the strut. The orthoslices image of $X - Z$ plane was used for determining strut dimensions to minimise the influence of surface condition. Twenty different locations were investigated per each 2D image to extract the mean values for the strut length and diameter.

It was found that good accuracy was achieved by the lattice manufacturing process for the strut length,l, however the measured strut diameter d ranged from 0.79mm to 0.82mm, significantly higher than the original design, see Tab.1. The porosity was evaluated by isolating the pore areas within the matrix, shown in Fig.6(b). The volume of the pore area and the scanned matrix were both evaluated to calculate a sample porosity which was equal to 2.2%.

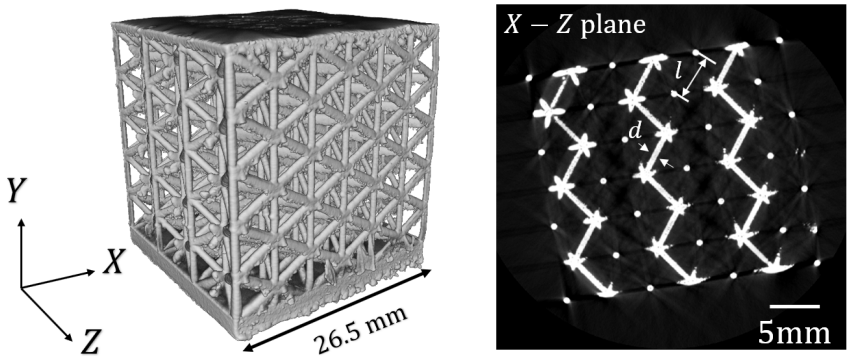

(a) (b)

Figure 5: Result of X-ray computed tomography with low magnification:(a) volume of the entire sample probed; (b) typical 2D orthoslice image (X-Z plane) of the sample across its height (Y-axis)

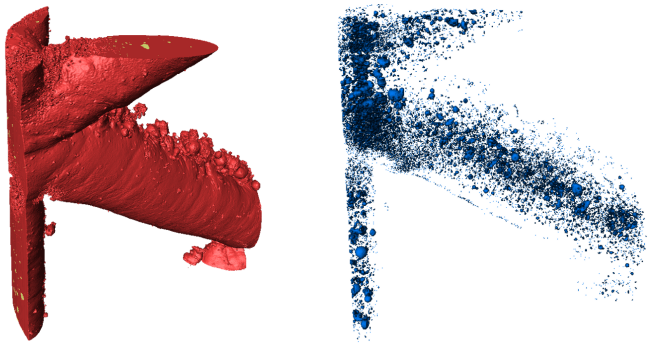

(a) (b)

Figure 6: 3D volume of the sample being probed using high magnification:(a) entire probed volume illustrating the exterior surface (pores and matrix shown in yellow and red colour respectively; (b) pore network within the scanned area

	diameter,d	Strut length,l	Relative density, $\overline{\rho}$	Porosity
Nominal	0.5mm	5mm	0.067	2.2%
Measured	0.79-0.82mm	5mm	0.17	

Table 1: Measured strut dimensions and porosity

2.4. Tensile test

A solid round bar specimen was chosen for the tensile test to determine the material stress-strain response. Measuring the response of a single strut cut from the specimen was discounted because the surface roughness of the strut would result in significant uncertainty of the cross-sectional area. The round bar was manufactured using the same process parameter as the CT specimens to a standard dog-bone geometry with gauge length of 25mm and diameter of 6mm.The sample was built vertically along the build direction. The strain was measured by 25mm Instron extensometer[32] and the stress-strain curve is shown in Fig.7. The modulus and ultimate tensile strength were measured to be 63 GPa and 320 MPa. It was found that the modulus was lower than would be expected for an aluminium alloy, likely to be caused by porosity within the specimen[33, 34] and the built orientation[35].

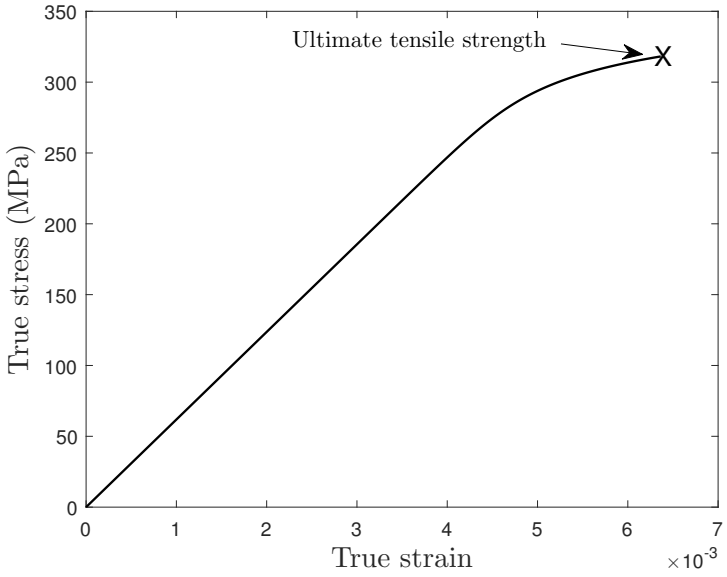

Figure 7: stress-strain curve of parent material measured from round bar tensile test

2.5. Fracture test

Fracture tests were carried out using the apparatus shown in Fig.8. A periodic loading pattern was used so that the specimen compliance could be measured as the crack extended. In each cycle, loading was applied so that the crack mouth opening displacement (CMOD) increased by 0.5mm followed by unloading to reduce the CMOD by 0.25mm. This pattern of loading allowed small increment of displacement to be applied to the specimen, aiming to capture as many as possible analysis points on the Load-CMOD curve[36]. The rate of loading and unloading were set to 0.2mm/min, to maintain a static deformation rate[37]. Instron 2670-132 extensometer[38] with gauge length 10 mm was installed at the specimen knife edges to measure crack mouth opening displacement (CMOD). The crack extension was tracked by an iMETRUM video gauge system [39].

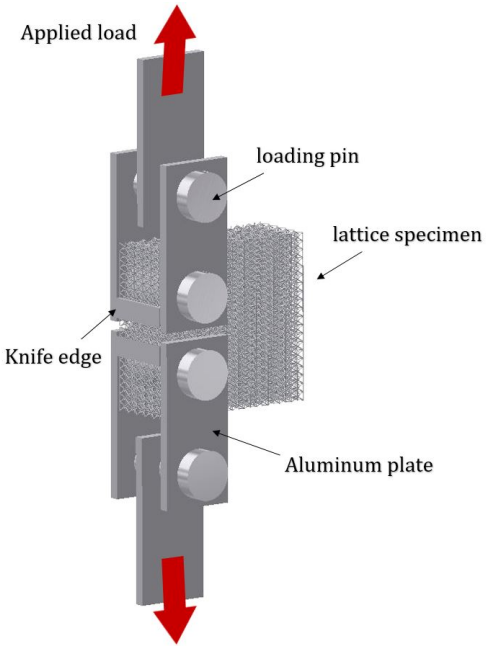

Figure 8: Experiment set up

3. Results

Fracture tests have been conducted using two orientation-y specimens and three orientation-z specimens. The load-displacement responses are shown in Fig.9 and 10. There is reasonably good repeatability, particularly for the peak load. Fig.11 compares load-displacement curves for different orientations: orientation-y (specimen 2) and orientation-z (specimen 3). An increase in critical load can be observed for both orientations with crack extension. The point a in Fig.11 indicates the initial critical load where failure was observed at struts ahead of the initial crack tip, while point b indicates the peak load. Struts A and B in Fig.12 shows the location of failed struts corresponding to points a and point b in Fig 11. For the orientation-y specimen, the angled strut at location A failed first without a noticeable drop in load. A significant drop in load was observed when vertical struts at location B failed. A similar behaviour occurred for orientation-z specimens. Despite the significant surface roughness observed from the images of X-ray computed tomography which could result in variation of strength along the strut, the failure location of each strut was found to be almost consistent. Most failures occurred at the location near to the joint caused by the influence of strut bending and local stress concentration shown in Fig.16 and 17.

Repeatable crack paths were observed for each specimen, as shown in Fig 13. The crack of orientation-y specimens deviated after initiation and the entire crack plane was rotated by 30° about the Z-axis. The crack path for orientation-z specimens was almost horizontal.

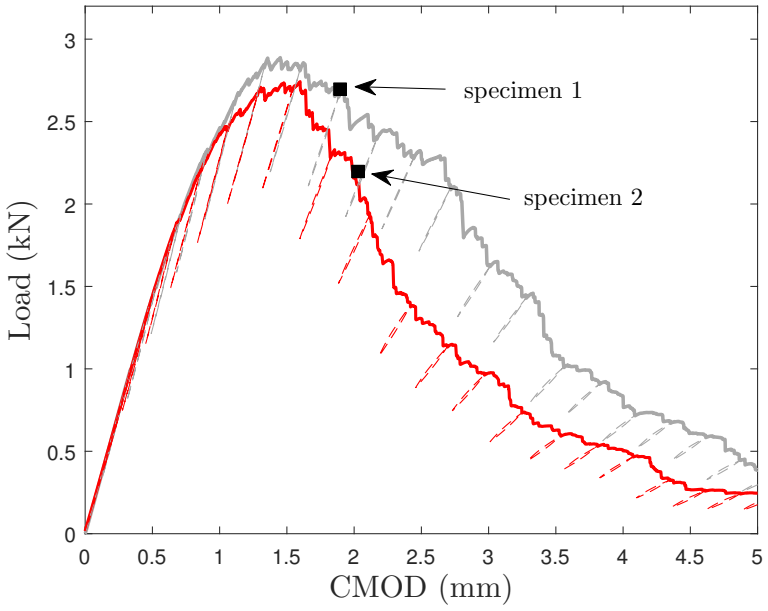

Figure 9: Load-displacement response of orientation-y specimen

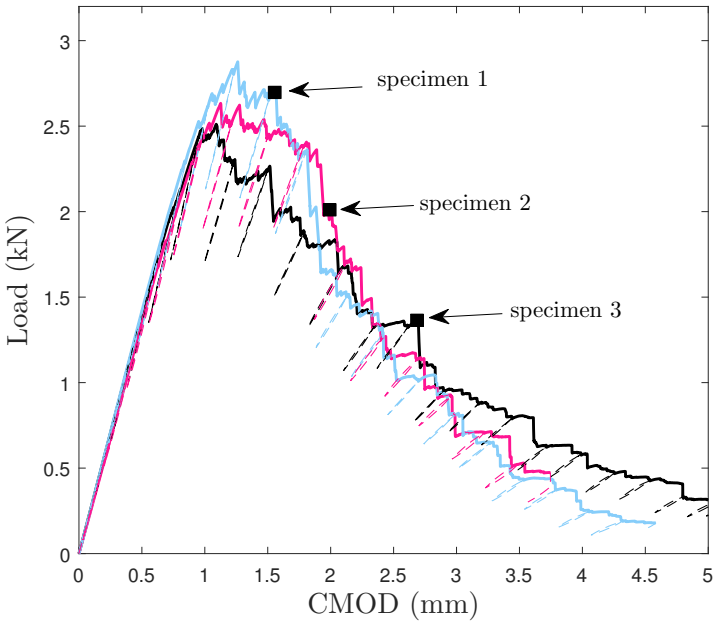

Figure 10: Load-displacement response of orientation-z specimen

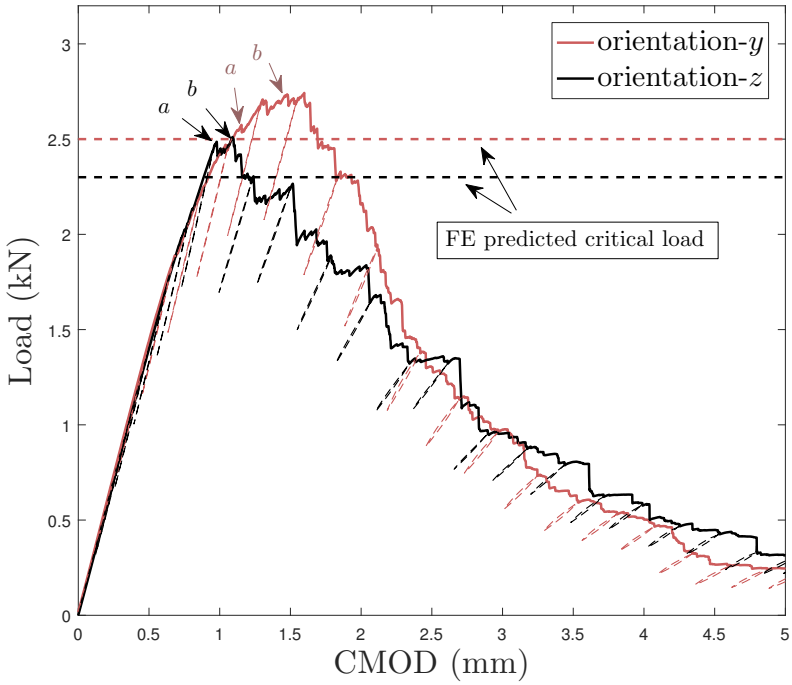

Figure 11: Load-displacement response of lattice specimens for two orientations: the results are compared between specimen 2 from orientation-y and specimen 3 from orientation-z

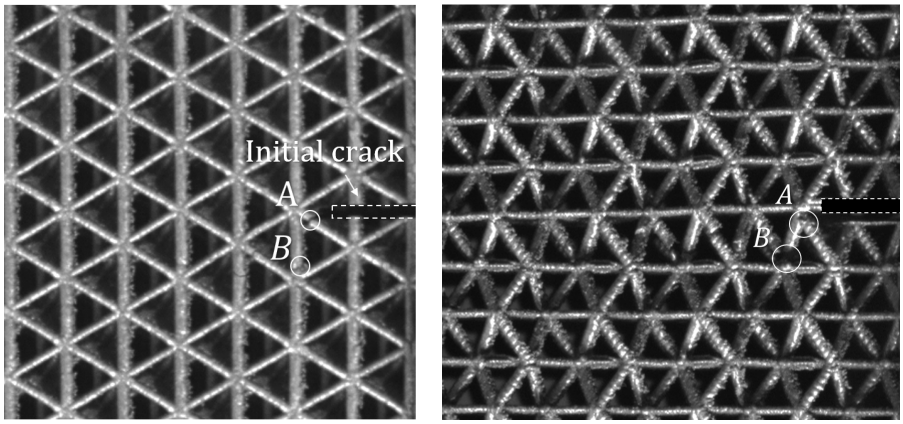

(a) (b)

Figure 12: Details of crack growth of orientation-y specimen

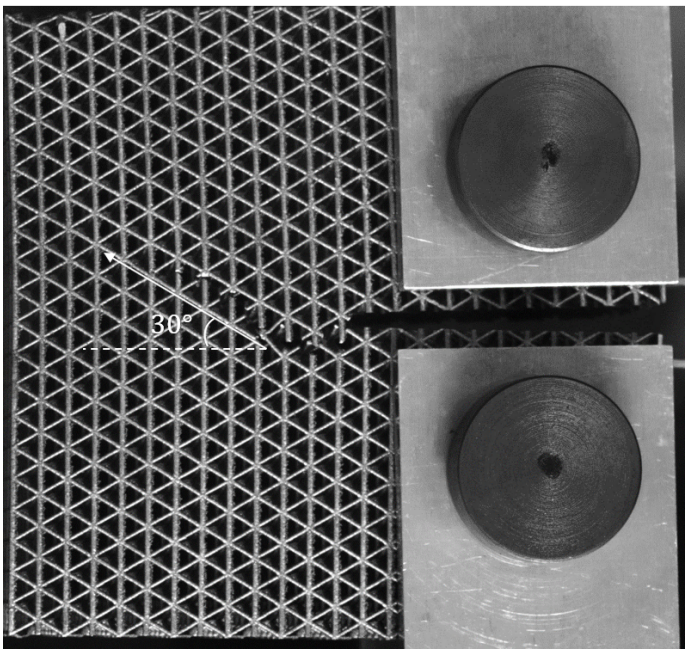

(a)

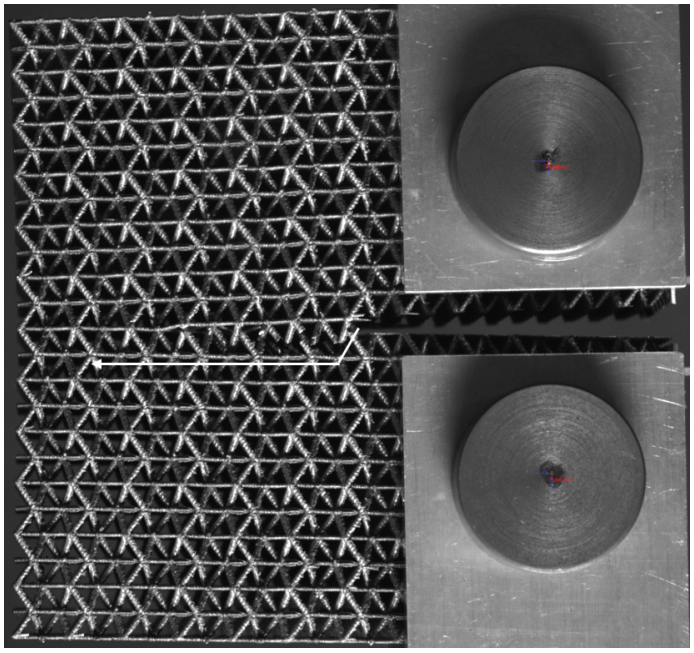

(b)

Figure 13: Crack path observed for (a) orientation-y and (b) orientation-z

The compliance of each specimen was calculated using the slope of each unloading during crack extension (the dashed lines in Fig.9 and 10). The effective crack length, a/W, can be calculated from the compliance using the ASTM E399 standard [26]:

$$\frac{a}{W} = 1.000 - 4.500U + 13.157U^2 - 172.551U^3 + 879.944U^4 - 1514.6711U^5 \quad (3)$$

and:

$$U = \frac{1}{1 + \sqrt{(\frac{EBV_m}{P})}} \quad (4)$$

where V_m is the crack mouth opening displacement, P the applied force, B is the specimen thickness and E is the equivalent Young's modulus of the lattice which was calculated based on the measured relative density,$\overline{\rho}$, using the expression given in [40]. The effective crack length matched adequately with visual observations for orientation-z specimens. For the orientation-y specimens, the observed crack length was found to be significantly longer than the effective crack length. When the crack significantly deviated from the horizontal plane, the compliance method was inappropriate for the prediction of the crack length due to the assumption made in the ASTM standard. Fig.14 shows fracture resistance, K_R, with increasing normalised effective crack length. The fracture resistance is calculated as:

$$K_R = \frac{P_m}{B\sqrt{W}} f(\frac{a}{W}) \quad (5)$$

with:

$$f(\frac{a}{W}) = \frac{(2 + \frac{a}{W})[0.886 + 4.64(\frac{a}{W})^2 - 13.32(\frac{a}{W})^3 - 5.6(\frac{a}{W})^4]}{(1 - \frac{a}{W})^{3/2}} \quad (6)$$

where P_m is the maximum applied load in each load cycle. The fracture resistance for crack onset was found to be similar for the two orientations of specimen. An increase in K_R with crack growth was also observed for both orientations after crack initiation, as shown in Fig.14.

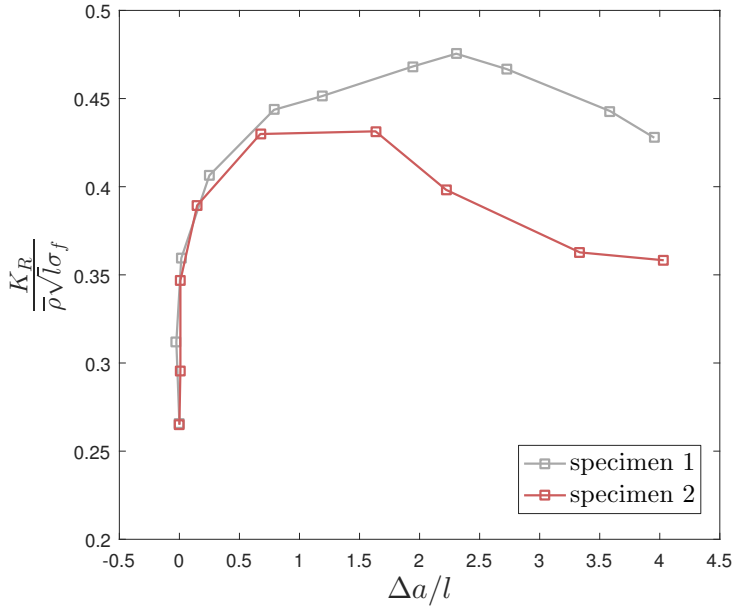

(a)

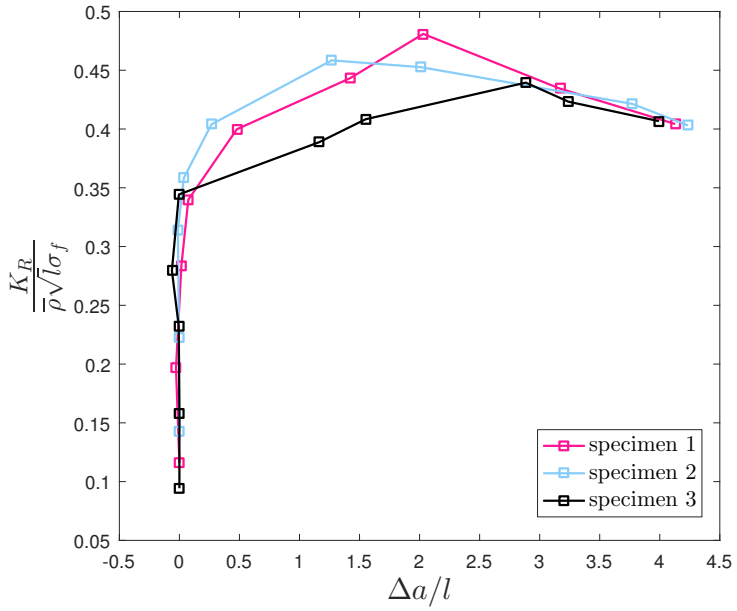

(b)

Figure 14: Fracture resistance,K_R, of lattices with (a)orientation-y and (b)orientation-z

4. FE evaluation

FE analysis was performed using Abaqus 6.14 to predict fracture properties of the lattice. Each strut was modelled using 5 Euler-Bernoulli beam elements (Abaqus element type B33), which was found to be sufficient to achieve a converged solution. Models created for both orientation-y and orientation-z specimens contained approximately 270, 000 nodes and 150, 000 elements. The material behaviour was described by the Ramberg-Osgood relationship:

$$\varepsilon = \frac{\sigma}{E} + 0.002\frac{\sigma}{E}(\frac{\sigma}{\sigma_y})^{n-1} \tag{7}$$

The Young's modulus $E = 63$GPa. The yield strength,σ_y, and hardening coefficient,n, are chosen to be 245 MPa and 20 to approximate the stress-strain curve measured from the tensile test shown in the Fig.7. The cell dimensions were defined based on the results of the X-ray computed tomography presented in Sec.2. The significance of build orientation on the mechanical properties have been investigated previously [20]. However, strut properties assumed to be identical in this study for the ease of modelling. The motion of nodes around each pin hole was firstly coupled to a controlling point defined at the hole center. A fixed displacement was then applied at the controlling point to replicate the experiment arrangement.

The failure condition used in this study depends on the magnitude of axial stress: the element is considered to have failed when the maximum axial stress across the element section reaches the tensile strength measured in the tensile test described in Sec.2.4. This failure condition was chosen due to the relative brittle behaviour exhibited by the aluminium alloy. The critical load on the model was evaluated when the failure condition was met at the most heavily loaded strut. It was found the strut at the crack tip was subjected to both tensile and bending stresses. A significant bending stress was found in the orientation-z models due to the large angle between the strut and the loading directions, which causes the lower critical load compared to that of the orientation-y model. The FE predicted critical load is plotted in Fig.11 and compared to the experimental

measurements with good agreement.

The failed elements were then removed from the model, and the same boundary conditions applied to predict the locations of the next failed elements and the corresponding critical loads. In this way, the crack paths for orientation-y and orientation-z specimens were predicted, as shown in Fig. 15. There is close agreement with the experiment results shown in Fig.13.

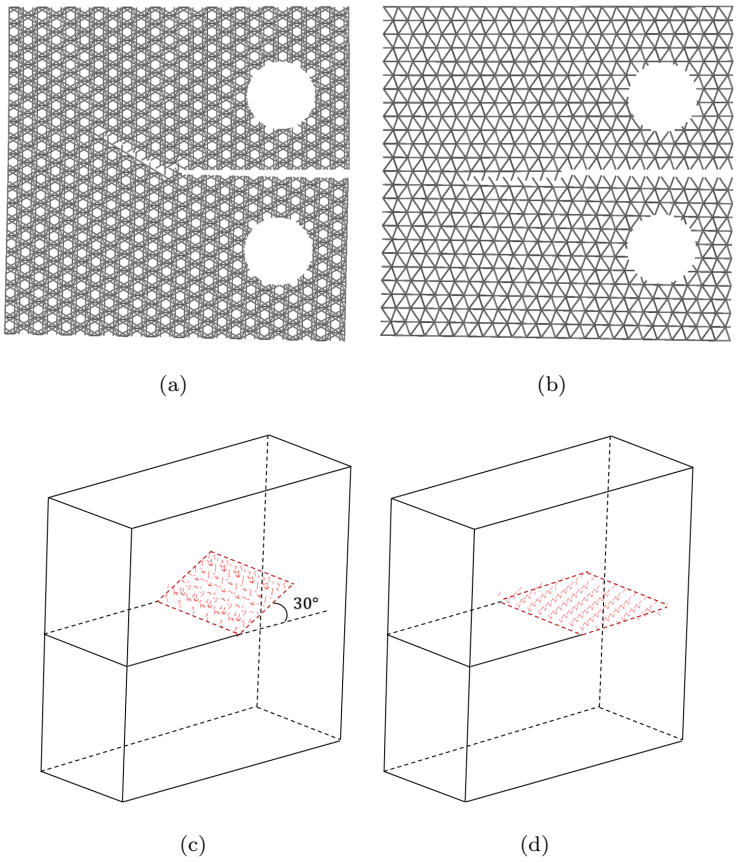

Figure 15: Crack path predicted from FE analysis: (a)for orientation-y and (b) for orientation-z show a side view of the models after failed elements have been removed;(c)for orientation-y and (d) for orientation-z show the elements that have failed in a perspective view.

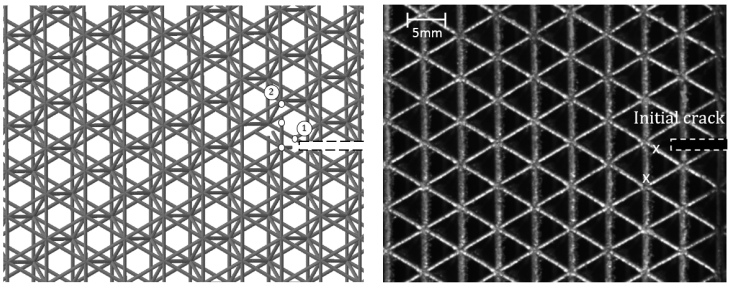

(a) CMOD=1.5mm

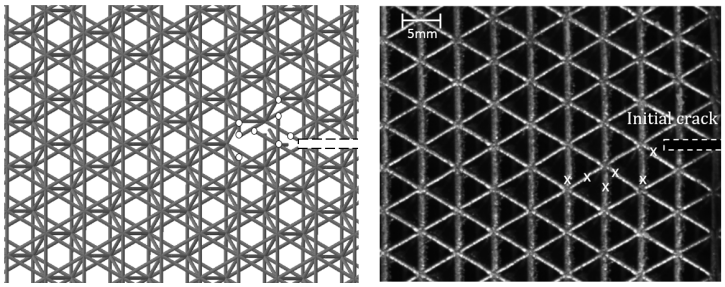

(b) CMOD=2.0mm

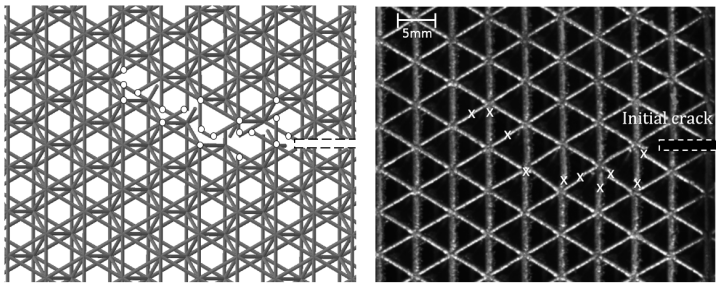

(c) CMOD=2.3mm

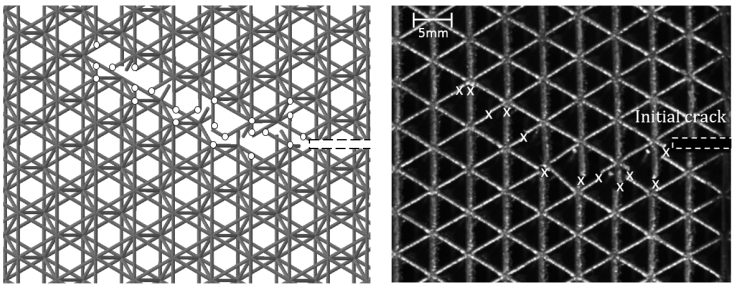

(d) CMOD=2.7mm

Figure 16: Details of crack growth of orientation-y specimen

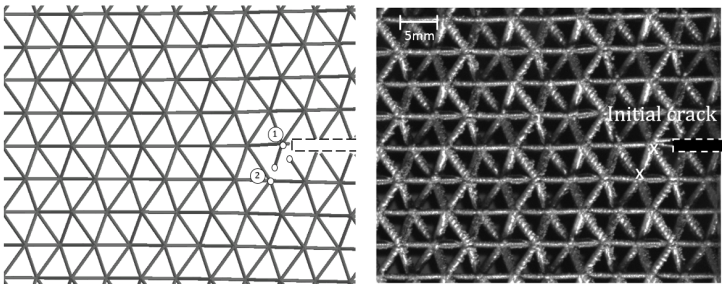

(a) CMOD=1.4mm

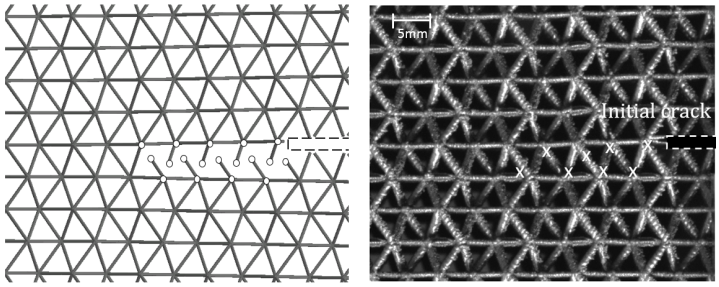

(b) CMOD=2.0mm

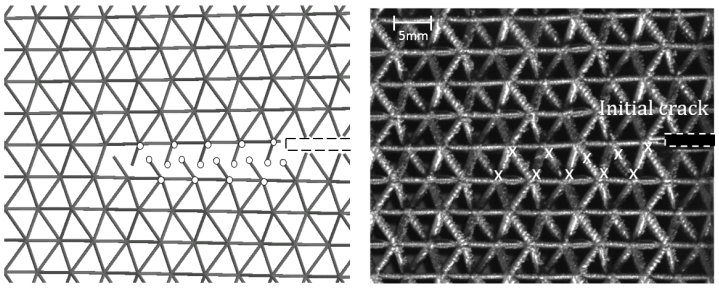

(c) CMOD=2.5mm

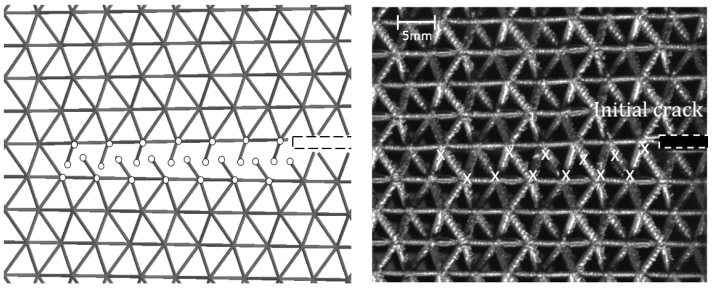

(d) CMOD=2.8mm

Figure 17: Details of crack growth of orientation-z specimen

Fig.16 and 17 compare the FE predicted crack path with the experimental observation. The labels in Fig.16(a) and 17(a) indicate the first and second location of element failure in the models. The critical loads were found to increase by 3% after struts failed at the first location for the orientation-y model and 7% for orientation-z model. This was similar to the experiment observations described in Sec.3 and Fig.11. In the orientation-y model, the angled struts failed first and the peak load was not reached until the vertical struts at the second location reached their maximum loading capacity. Hence, the peak load is controlled mainly by the strength of vertical struts ahead of the crack front.

For the orientation-z model, there are no struts parallel to the loading direction. However, it was found that the maximum axial stress in the model reduces as failed elements are removed in front of the initial crack front. This, indicates that a stronger tip configuration is formed after crack initiation and thus a higher load is required to re-initiate the crack.

The stress intensity at initiation, K_I , was calculated by substituting the predicted initial critical load into Eqn.(4), and the results were shown in Table.2. It was found that a very similar result was calculated for both lattice orientations.

	orientation-y	orientation-z
Measured results	0.35	0.34
	0.36	0.35
		0.36
FE prediction	0.34	0.32

Table 2: Comparison of normalised stress intensity, $\frac{K_I}{\bar{\rho}\sigma_f\sqrt{l}}$, at crack initiation between experimental measurements and FE predictions

A set of FE analyses were performed on 5 different sized models with W ranging from $8.5l$ to $42l$ (shown in Fig.18) to demonstrate the effect of specimen size on the stress intensity at failure. The critical load and K_I for crack initiation was evaluated for each model. Fig.19 plots the normalised stress intensity, K_I,

at failure against normalised model size. It was found that K_I reduces with increasing model size for both lattice orientations. This can be attributed to the increase in constraint at the crack tip, which causes a triaxial state of stress leading to an increase in the axial stress in the most heavily loaded strut. It was found that the orientation-y model exhibited a significantly higher size dependency compared that to that of the orientation-z model. This is because the load is predominantly carried by the layers of triangular lattices in the orientation-y model shown in the Fig.1. The number of the equally spaced layer increases with model size, leading to the reduction of effective strength of the overall structure. However, it was noticed that the two sets of results were asymptotic to almost the same value with increasing model size.

The largest model was created with $W = 42l$, which contained about 2.5 million nodes and 1.4 million elements. About 29 gigabytes of memory was required for the analysis. No attempt was made to analyse a larger model. However, a previous study on two-dimensional triangular lattices [13] showed that a lattice model with $W = 42l$ is large enough to provide a prediction of the fracture toughness. The stress intensity at fracture for the lattice model with $W = 42l$ shown in Fig.19 can therefore be taken to be equal to the fracture toughness, K_{IC}. The results also indicate that for the specimen size used in the experiment ($W = 17l$), the measured K_I at initiation is approximately 10% higher than the fracture toughness,K_{IC}.

The scaling relationship between the relative density,$\overline{\rho}$, and fracture toughness, K_{IC} is illustrated in Fig.20. The results were evaluated from a set of orientation-y models created with $W = 42l$, sufficiently large to eliminate the influence of model size. The strut length,l, remained constant, while the radius,r, was varied from 0.1mm to 0.6mm. Fig.20 confirms the fracture toughness of the lattice scales linearly with the relative density,$\overline{\rho}$. Hence, the fracture toughness,K_{IC}, of both orientation-y and orientation-z lattices scale as:

$$K_{IC} = 0.3\overline{\rho}\sigma_f\sqrt{l} \tag{8}$$

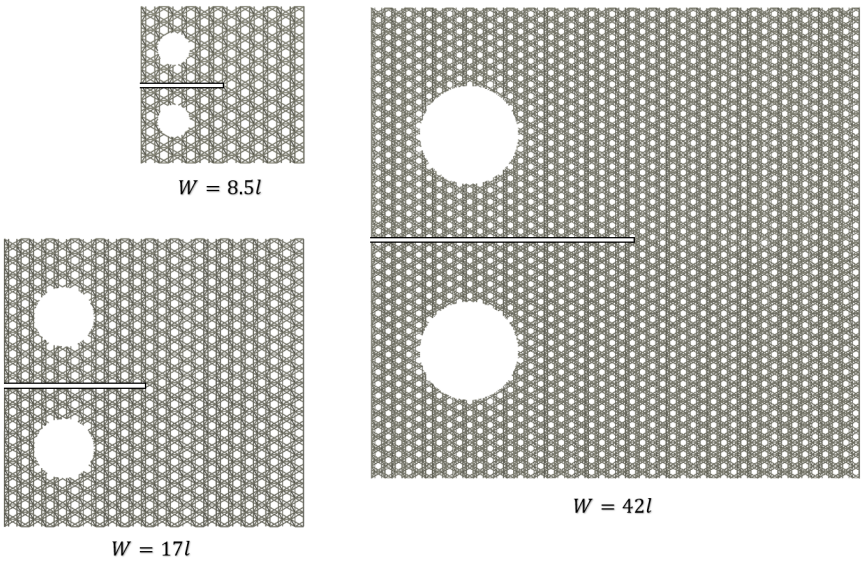

Figure 18: Lattice models created in different sizes

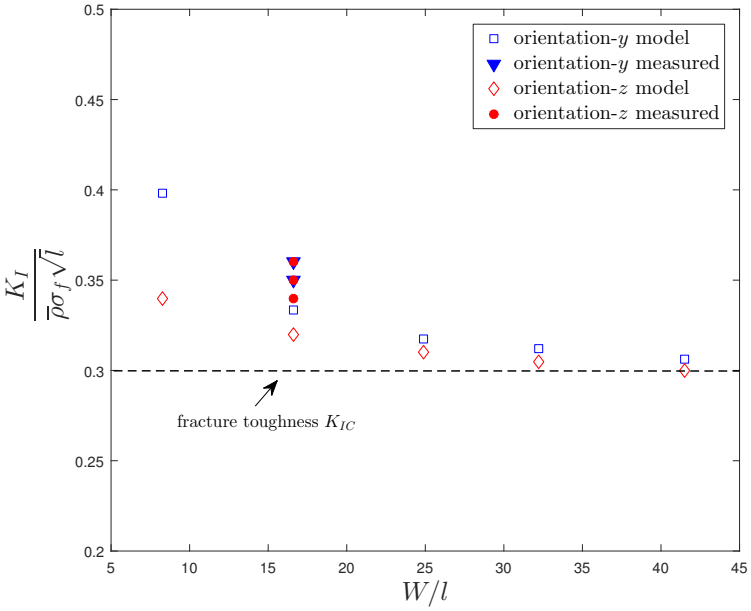

Figure 19: Effect of specimen size on toughness measurement

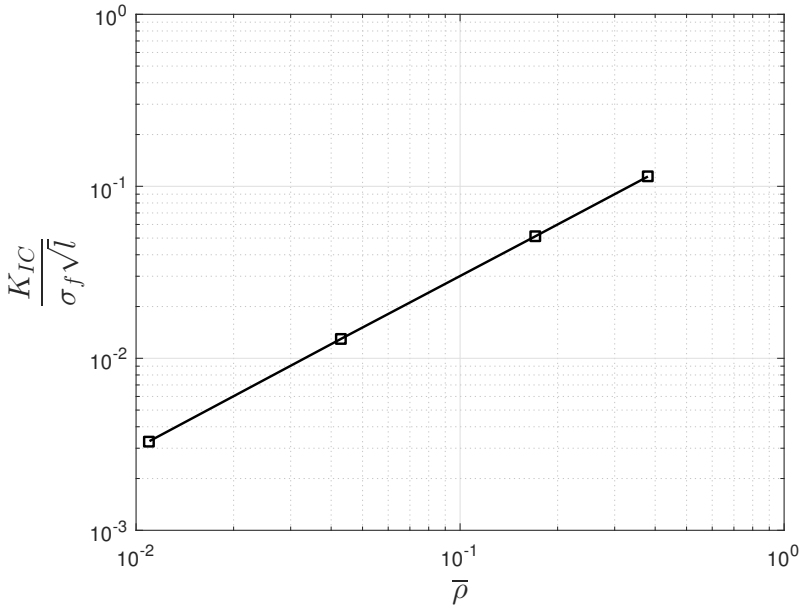

Figure 20: The scaling relationship between relative density and fracture toughness of the lattice

5. Discussion

The current results show that the orientation-y and orientation-z lattices exhibit almost identical fracture toughness,K_{IC}. By using the same numerical approach, we investigated the fracture toughness of the octet-truss lattices in two different orientations referred to as orientation-x and orientation-FCC shown in Fig 21. In the orientation-x model, the unit cell was rotated by 90° about the y-axis relative to the unit cell of the orientation-z model. The x-axis of the local coordinate system is aligned with the loading direction. The orientation-FCC is a face-centred cubic structure, and the loading is applied along the [1 0 0] direction according to the coordinate system defined by Dong et al.[27].

The models were created with $W = 42l$ in order to achieve the asymptotic toughness value. Tab.3 compared the evaluated fracture toughness for each lattice orientation. It was found the toughness of the orientation-x and

orientation-FCC were very similar compared to that of the orientation-y and orientation-z models. A small discrepancy between the evaluated toughness was associated with the different level of strut bending exhibited at the crack tip. The bending stress at crack tip was relatively large in the orientation-FCC model compared to other orientations due to the large angle between the strut and loading directions. This causes a higher axial stress and results in the reduction in its toughness.

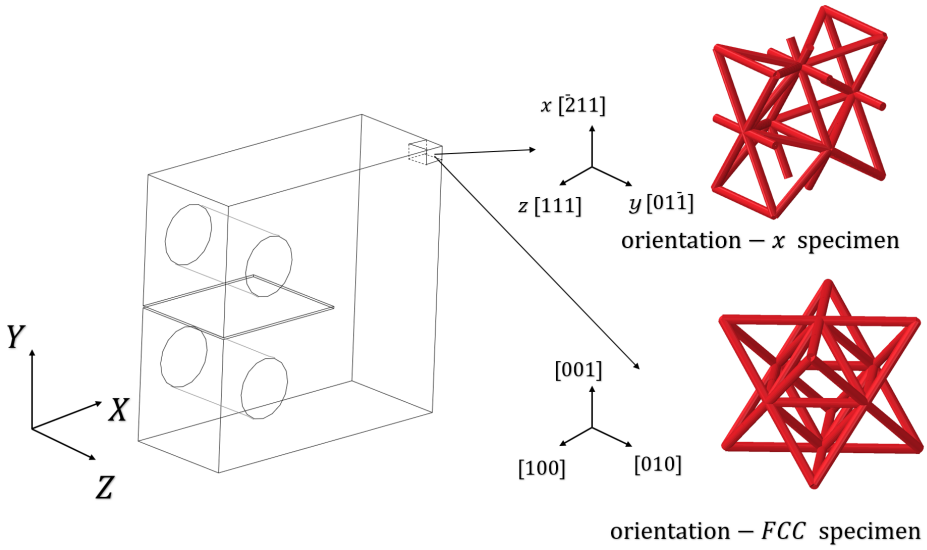

Figure 21: Compact tension models for orientation-x and orientation-FCC

	orientation-x	orientation-y	orientation-z	orientation-FCC
$\frac{K_{IC}}{\bar{\rho}\sigma_f\sqrt{l}}$	0.31	0.3	0.3	0.29

Table 3: Evaluated fracture toughness of octet-truss lattice for different orientations.

The fracture toughness of the orientation-FCC structure fabricated using Ti-6Al-4V alloy was experimentally measured by M.O'Masta et.al.[18] through a three-point bending fracture test. Compared to the single edge notch bend(SENB) specimen, compact tension(CT) specimen allows crack to grow in a stable manner which enables monitoring of the change of fracture resistance,K_R, during

crack extension[26]. However, the CT specimen used in this study involves both solid and lattice regimes which causes stress concentration at the interfaces. This could be a potential concern for conducting test using a specimen with small a/W, where the strut in vicinity to the pin might fail prior to crack initiation.

Fig.22 illustrates the fracture toughness measured in the present study and the results reported by M.O'Masta et.al in the material property chart. It shows that the A205 aluminium octet-truss lattice reached to a comparable toughness value to the Titanium lattices, which is superior compared to that of foams and nature materials at this density.

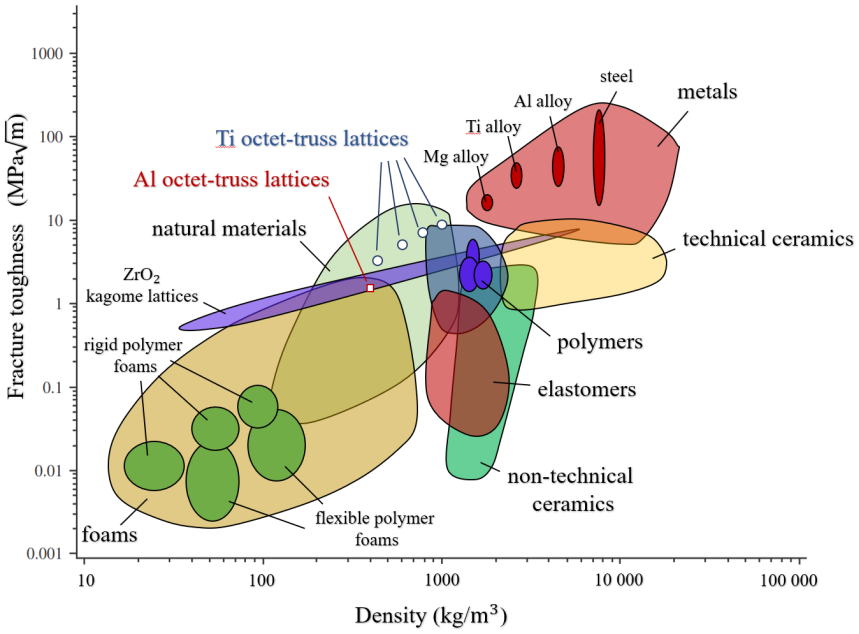

Figure 22: Material property chart of the fracture toughness,K_{IC}, against density. The property values were sourced from [41], and the fracture toughness of Ti octet-truss lattice was based on the measurement from M.O'Masta et.al.[18].

6. Conclusion

The fracture behaviour of octet-truss lattices has been investigated experimentally for two orientations of the lattice relative to the loading direction. The fracture resistance, crack path and load-displacement curves have been measured. For both orientations, the fracture resistance increases with crack extension. A change in lattice orientation resulted in significant effect on the crack path, but little effect on the fracture resistance. Finally, the results of numerical study on the size effect indicated that the fracture resistance measured in this study was about 10% larger than would be measured in a sufficiently large specimen.

References

[1] Zhou, P. Shrotriya, W. Soboyejo, On the deformation of aluminum lattice block structures: from struts to structures, Mechanics of Materials 4 (2004) 723 – 737.

[2] H. Alsalla, L. Hao, C. Smith, Cellular ti–6al–4v structures with interconnected macro porosity for bone implants fabricated by selective electron beam melting, Acta Biomaterialia 4 (2008) 1536 – 1544.

[3] A. K. Noor, S. L. Venneri, D. B. Paul, M. A. Hopkins, Structures technology for future aerospace systems, Computers and Structures 74 (2000) 507–519.

[4] K. V, The buckling response of lattice fuselage structures : Validation of finite element models by using smeared unit cell analytical methodology, Journal of Aeronautics Aerospace 6 (1) (2017) 1–5.

[5] Schaedler, T. A. and Jacobsen, A. J. and Torrents, A. and Sorensen, A. E. and Lian, J. and Greer, J. R. and Valdevit, L. and Carter, W. B., Ultralight metallic microlattices, American Association for the Advancement of Science 334 (2011) 962–965.

[6] Evans, K. E. and Alderson, A., Auxetic materials: Functional materials and structures from lateral thinking, Advanced Materials 12 (2000) 617–628.

[7] Wadley, Haydn N.G. and Queheillalt, Douglas T., Thermal Applications of Cellular Lattice Structures, Vol. 539 of Materials Science Forum, Trans Tech Publications, 2007.

[8] V. S. Deshpande, M. F. Ashby, N. A. Fleck, Foam topology: Bending versus stretching dominated architectures, Acta Materialia 49 (6) (2001) 1035–1040.

[9] A.-J. Wang, D. L. McDowell, In-Plane Stiffness and Yield Strength of Periodic Metal Honeycombs, Journal of Engineering Materials and Technology 126 (2) (2004) 137–156.

[10] I. Schmidt, N. A. Fleck, Ductile fracture of two-dimensional cellular structures, International Journal of Fracture 111 (4) (2001) 327–342.

[11] N. H.C.Tankasala, V.S.Deshpande, Crack-tip Fields and Toughness of Two-Dimensional Elasto-plastic Lattices, Journal of Applied Mechanics 82 (2015) 1–10.

[12] N. A. Fleck, X. Qiu, The damage tolerance of elastic-brittle, two-dimensional isotropic lattices, Journal of the Mechanics and Physics of Solids 55 (3) (2007) 562–588.

[13] H. Gu, M. Pavier, A. Shterenlikht, Experimental study of modulus, strength and toughness of 2d triangular lattices, International Journal of Solids and Structures.

[14] J. S. Huang, L. J. Gibson, Fracture toughness of brittle honeycombs, Acta metallurgica et materialia 39 (7) (1991) 1617–1626.

[15] P. Moongkhamklang, D. M. Elzey, H. N. Wadley, Titanium matrix composite lattice structures, Composites Part A: Applied Science and Manufacturing 39 (2008) 1264–1272.

[16] J. Liu, S. Pattofatto, D. Fang, F. Lu, H. Zhao, Impact strength enhancement of aluminum tetrahedral lattice truss core structures, International Journal of Impact Engineering 79 (2015) 3 – 13.

[17] H. N. G. W. K. Finnegan, G. Kooistra, V. S. Deshpande, The compressive response of carbon fiber composite pyramidal truss sandwich cores, International Journal of Materials Research 98 (2007) 1264–1272.

[18] M. O'Masta, L. Dong, L. St-Pierre, H. Wadley, V. Deshpande, The fracture toughness of octet-truss lattices, Journal of the Mechanics and Physics of Solids 60-61 (2017) 98.

[19] C. Qiu, S. Yue, N. J. Adkins, M. Ward, H. Hassanin, P. D. Lee, P. J. Withers, M. M. Attallah, Influence of processing conditions on strut structure

and compressive properties of cellular lattice structures fabricated by selective laser melting, Materials Science and Engineering: A 628 (2015) 188 – 197.

[20] R. Wauthle, B. Vrancken, B. Beynaerts, K. Jorissen, J. Schrooten, J.-P. Kruth, J. V. Humbeeck, Effects of build orientation and heat treatment on the microstructure and mechanical properties of selective laser melted ti6al4v lattice structures, Additive Manufacturing 5 (2015) 77 – 84.

[21] M. Leary, M. Mazur, J. Elambasseril, Selective laser melting (SLM) of AlSi12Mg lattice structures, Materials and Design 98 (2016) 344 – 357.

[22] C. Yan, L. Hao, A. Hussein, D. Raymont, Evaluations of cellular lattice structures manufactured using selective laser melting, International Journal of Machine Tools and Manufacture 62 (2012) 32 – 38.

[23] EI. Maskery and N.T. Aboulkhair and A.O. Aremu and C.J. Tuck and I.A. Ashcroft and R.D. Wildman and R.J.M. Hague, A mechanical property evaluation of graded density al-si10-mg lattice structures manufactured by selective laser melting, Materials Science and Engineering: A 670 (2016) 264 – 274.

[24] H. E. Burton, N. M. Eisenstein, B. M. Lawless, P. Jamshidi, M. A. Segarra, O. Addison, D. E. Shepherd, M. M. Attallah, L. M. Grover, S. C. Cox, The design of additively manufactured lattices to increase the functionality of medical implants, Materials Science and Engineering: C 94 (2018) 901 – 908.

[25] H. Alsalla, L. Hao, C. Smith, Fracture toughness and tensile strength of 316l stainless steel cellular lattice structures manufactured using the selective laser melting technique, Materials Science and Engineering: A 5 (2016) 1 – 6.

[26] ASTM E399 - 17-Standard Test Method for Linear-Elastic Plane-Strain

Fracture Toughness KIc of Metallic Materials, American Society for Testing and Materials.

[27] L. Dong, V. Deshpande, H. Wadley, Mechanical response of ti–6al–4v octet-truss lattice structures, International Journal of Solids and Structures 60-61 (2015) 107 – 124.

[28] E.Herny, J.Rideau, M. Attallah, Title of patent: Production of half-stages of monobloc stator guides by additive manufacturing, 2016-09-15.

[29] N. Aboulkhair, Additive manufacture of an aluminium alloy: processing, microstructure, and mechanical properties, Ph.D. thesis (12 2015).

[30] Ivan Zuiko and Rustam Kaibyshev, Aging behavior of an al–cu–mg alloy, Journal of Alloys and Compounds 759 (2018) 108 – 119.

[31] Avizo user guide, [ONLINE] Available at `https://assets.thermofisher.com/TFS-Assets/MSD/Product-Guides/user-guide-avizo-software.pdf`.

[32] Instron strain gauge extensometer product description 2017, [ONLINE] Available at `https://www.instron.us/en-us/products/testing-accessories/extensometers/axial-clip-on/static/2630-106`,.

[33] Choren, J. A., Young's modulus and volume porosity relationships for additive manufacturing applications, Journal of Materials Science 48 (2013) 5103–5112.

[34] M. Asmani and C. Kermel and A. Leriche and M. Ourak, Influence of porosity on young's modulus and poisson's ratio in alumina ceramics, Journal of the European Ceramic Society 670 (2001) 1081 – 1086.

[35] B. J. Mfusi, L. C. Tshabalala, A. P. I. Popoola, N. R. Mathe, The effect of selective laser melting build orientation on the mechanical properties of AlSi10mg parts, IOP Publishing 430.

[36] ASTM E1820 - 18-Standard Test Method for Measurement of Fracture Toughness, American Society for Testing and Materials.

[37] ASTM E561 - 17-Standard Test Method for KR Curve Determination, American Society for Testing and Materials.

[38] Instron extensometer product description 2017, [ONLINE] Available at http://www.instron.se/sv-se,.

[39] Imetrum.2012, Video GaugeTM - How it works [ONLINE] Available at: https://www.imetrum.com/video-gauge/how-it-works/.
URL https://www.imetrum.com/video-gauge/how-it-works/

[40] V. Deshpande, N. Fleck, M. Ashby, Effective properties of the octet-truss lattice material, Journal of the Mechanics and Physics of Solids 49 (2001) 7181 – 7196.

[41] N. A. Fleck, V. S. Deshpande, M. F. Ashby, Micro-architectured materials: past, present and future, Proceedings of the Royal Society A: Mathematical, Physical and Engineering Sciences 466 (2010) 2495–2516.